Single-domain spectral method for black hole puncture data

Marcus Ansorg, Bernd Brügmann, and Wolfgang Tichy
Center for Gravitational Physics and Geometry and Center for Gravitational Wave Physics, Penn State University, University Park, Pennsylvania 16802, USA
(Received 13 April 2004; published 7 September 2004)

We calculate puncture initial data corresponding to both single and binary black hole solutions of the constraint equations by means of a pseudospectral method applied in a single spatial domain. Introducing appropriate coordinates, these methods exhibit rapid convergence of the conformal factor and lead to highly accurate solutions. As an application we investigate small mass ratios of binary black holes and compare these with the corresponding test mass limit that we obtain through a semianalytical limiting procedure. In particular, we compare the binding energy of puncture data in this limit with that of a test particle in the Schwarzschild spacetime and find that it deviates by 50% from the Schwarzschild result at the innermost stable circular orbit of Schwarzschild, if the ADM mass at each puncture is used to define the local black hole masses.

DOI: 10.1103/PhysRevD.70.064011 PACS numbers: 04.25.Dm, 04.20.Ex, 95.30.Sf

I. INTRODUCTION

The evolution problem of general relativity requires the specification of initial data that satisfies the Hamiltonian and momentum constraints on the initial hypersurface. There are different strategies to pose initial data for a specific physical situation, which typically involve a choice of free data and the subsequent numerical solution of the constraint equations to obtain the physical data; see [1] for a recent review. An active area of research is concerned with initial data that describe two orbiting black holes [2–6]. For example, one can study the two-body problem of relativity by constructing sequences of quasicircular binary data sets that describe the quasiadiabatic inspiral of two black holes [7–14]. Furthermore, binary black hole data sets are the starting point for evolutions in numerical relativity, e.g., [15].

Important aspects of black hole data sets are the choice of hypersurface and how the physical singularity inside the black holes is treated. Concretely, since the constraints give rise to elliptic equations, one has to specify a computational domain and boundary conditions. One possibility when considering two black holes is to work on $\mathbb{R}^3$ with two balls excised. At the spherical excision boundary one can impose boundary conditions based on an isometry, as suggested by Misner [16]. This boundary condition is used in the first fully 3D numerical data sets [2] and in the more recent thin sandwich-type initial data sets [11]. The excision boundary can also be defined by an apparent horizon boundary condition [17,18]; see [10,19] for recent applications. Other boundary conditions are motivated by Kerr-Schild coordinates [4].

Excising spheres introduces a technical complication into numerical methods on Cartesian grids. In finite differencing codes on Cartesian grids, the boundary points are not aligned with the grid and one has to construct appropriate stencils for a "lego" sphere [2,20,21]. Alternatively, one can work with adapted coordinates which match the spherical boundary, for example, Čadež coordinates [2], or one can use multiple coordinate patches with spherical coordinates at the excision region [11,12,17–19].

An alternative to excision boundaries is to work on $\mathbb{R}^3$ with two points (the "punctures") excised, where the punctures represent the inner asymptotically flat infinity (Brill-Lindquist topology [22,23]). Using the Brill-Lindquist topology directly is problematic numerically since one has to resolve a one over radius coordinate singularity. However, it is possible to analytically compactify the inner asymptotically flat region, filling in the missing puncture points, and to work on $\mathbb{R}^3$ [3,24–27]. This simplifies the numerical method because no special inner boundary condition has to be considered [3].

In this paper we focus on the construction of an efficient numerical method for the computation of black hole puncture data for vacuum spacetimes containing one or two black holes with linear momentum and spin. The numerical method, pseudospectral collocation, e.g., [28], can give exponential convergence when the solution is infinitely often differentiable (C^∞). However, in its usual form puncture data is only C^2 at the punctures. We resolve this issue by constructing an appropriate coordinate transformation that renders the puncture data smooth at the location of the punctures. Consequently, our pseudospectral method converges rapidly to highly accurate solutions, although the convergence rate is generally not exponential due to logarithmic terms in expansions at infinity (see below).

Note that spectral methods have already been applied successfully to various elliptic problems in numerical relativity, including neutron star initial data [29–32], homogeneous star models [33,34], relativistic Dyson rings [35], and black hole initial data [5,11,12,19]. In particular, [11,19] use several coordinate patches to cover a binary black hole excision domain, and the situation can become quite complicated with 43 rectangular boxes and

three spherical shells with various overlap and matching boundary conditions [19]. While such multipatch codes have a certain grid adaptivity built-in (compare "spectral elements" [28]), one of our motivations was to simplify the spectral method by construction of a simpler computational domain.

Therefore, a noteworthy feature of our spectral puncture method is that our choice of coordinates maps $\mathbb{R}^3$, including spatial infinity and the two-puncture points, to a *single* rectangular coordinate patch. This is the case for spherical coordinates with a radial compactification, but recall that in addition we want to ensure smoothness at the punctures.

The paper is organized as follows. In Sec. II we describe our spectral method for the solution of the Hamiltonian constraint on a single domain. After we introduce the puncture data in Sec. III, Sec. IV discusses analytical issues and numerical results for a single puncture. In Sec. V we develop our single-domain spectral method for two punctures and present the key result, which is rapid convergence of this scheme to highly accurate solutions. The application of our method to the case of small mass ratios and a comparison with a semianalytic test mass limit can be found in Sec. VI. Finally, in Sec. VII we compute binding energies of puncture data in this limit. We conclude in Sec. VIII.

II. THE SPECTRAL METHOD

As will be discussed in detail in the subsequent sections, for both the single and the two-puncture initial data problems an elliptic equation of the form

$$f(u) \equiv \triangle u + \varrho(u) = 0 \tag{1}$$

arises for a function u. Here, $\triangle$ denotes the Laplace operator, and ϱ is a source term which in general depends on u.

In what follows we will introduce coordinates (A, B, φ) with

$$A \in [0, 1], \qquad B \in [-1, 1], \qquad \varphi \in [0, 2\pi), \tag{2}$$

for each specific case that we consider, in which u is well defined within the spatial domain, in particular, at its boundaries.

As will become clear below, u always obeys a physical falloff condition at spatial infinity,

$$\lim_{r\to\infty} u = 0. \tag{3}$$

Since in all cases to be considered the coordinate A is introduced such that

$$r \to \infty \Longleftrightarrow A \to 1, \tag{4}$$

we consider an additional function U which is given by

$$u = (A - 1)U. \tag{5}$$

In our spectral method, the values of this function U are calculated at the grid points (A_i, B_j, φ_k), i.e.,

$$U_{ijk} = U(A_i, B_j, \varphi_k), \tag{6}$$

$$0 \le i < n_A, \qquad 0 \le j < n_B, \qquad 0 \le k < n_\varphi, \tag{7}$$

where we choose

$$A_i = \sin^2\left[\frac{\pi}{2n_A}\left(i + \frac{1}{2}\right)\right], \tag{8}$$

$$B_j = -\cos\left[\frac{\pi}{n_B}\left(j + \frac{1}{2}\right)\right], \tag{9}$$

$$\varphi_k = 2\pi\frac{k}{n_\varphi}. \tag{10}$$

Hence, the grid points A_i and B_j are the zeros of the Chebyshev polynomials $T_{n_A}(1 - 2x)$ and $T_{n_B}(-x)$, respectively, whereas the φ_k represent the zeros of $\sin(n_\varphi\varphi)$. Our spectral expansion is thus a Chebyshev expansion with respect to the coordinates A and B, and a Fourier expansion with respect to φ.

The spectral method enables us to calculate first and second derivatives of U from the values U_{ijk} at the above grid points within the chosen approximation order which is given by the numbers (n_A, n_B, n_φ). Thus, for a vector

$$\vec{U} = (U_{000}, \ldots, U_{(n_A-1)(n_B-1)(n_\varphi-1)})^T \tag{11}$$

we may fill another vector

$$\vec{f}(\vec{U}) = (f_{000}, \ldots, f_{(n_A-1)(n_B-1)(n_\varphi-1)})^T \tag{12}$$

by the evaluation of $f(u)$ at the grid points (A_i, B_j, φ_k). This results in a nonlinear set of simultaneous equations

$$\vec{f}(\vec{U}) = 0 \tag{13}$$

for the unknown U_{ijk}.

For the function U we find particular boundary constraints by considering the elliptic Eq. (1), written in terms of (A, B, φ) at $A = 0$, $A = 1$, $B = \pm 1$. A solution U that is regular with respect to A, B and φ must obey these requirements, which therefore replace boundary conditions that usually need to be imposed. These boundary constraints are called "behavioral" [28]. In addition, a desired 2π periodicity with respect to φ is already "built-in" by the particular choice of our basis functions. Accordingly, using the spectral method with the above *interior* collocation points, no further work with respect to the boundaries needs to be done, for regularity and periodicity will be realized automatically. Hence, there is no other requirement constraining the function U. It is uniquely determined by the elliptic Eq. (1).

For the numerical solution of the discrete equivalent, Eq. (13), we address its nonlinearity by performing

Newton-Raphson iterations. The solution $\vec{U}$ is written as

$$\vec{U} = \lim_{N\to\infty} \vec{U}_N, \tag{14}$$

$$\vec{U}_{N+1} = \vec{U}_N - \vec{V}_N, \tag{15}$$

where $\vec{V}_N$ satisfies the linear problem

$$J_N \vec{V}_N = \vec{b}_N \tag{16}$$

with

$$J_N = \frac{\partial \vec{f}}{\partial \vec{U}}(\vec{U}_N), \qquad \vec{b}_N = \vec{f}(\vec{U}_N). \tag{17}$$

There are different ways to solve the linear system arising from multidimensional spectral methods, although some effort has to be made to obtain an efficient method since the one-dimensional spectral differentiation matrices are not sparse and the conditioning of the system can be problematic; see for example [19,28]. We solve (16) with the preconditioned "biconjugate gradient stabilized (BICSTAB)" method [36], and the choice of preconditioner is crucial for the overall efficiency of the method.

We construct a preconditioner which is based on a second order finite difference representation of J_N. To this end we consider the linearized differential equation corresponding to (1) on the equidistant grid in coordinates (α, β, φ) with

$$A = \sin^2\alpha, \qquad B = -\cos\beta. \tag{18}$$

Apart from the uniform distribution of our grid points, these coordinates have the additional advantage that U becomes symmetric with respect to the planes $\alpha = 0$, $\alpha = \pi/2$, $\beta = 0$ and $\beta = \pi$. Therefore, it is possible to calculate second order finite differencing approximations of first and second derivatives at any grid point by taking into account adjacent neighboring points only.

The resulting matrix has at most seven nonvanishing entries per row and is therefore well suited for the application of a sparse system solver. We use the program package HYPRE which offers a variety of sparse matrix methods [37]. A choice that works well in this context is the "generalized minimal residual" method preconditioned with the algebraic multigrid code "BOOMERAMG" [37].

Our implementation of the above procedure uses the BAM code as infrastructure [15]. Although both BAM and HYPRE support parallelization, we have not parallelized the elliptic solves for our spectral method. Computation of the binary black hole solution shown in Fig. 5 (below) takes four minutes on a Xeon/Linux workstation.

In what follows we evaluate the convergence of the spectral method by computing the "global relative accuracy" defined by

$$\delta_{n,m}(U) = \max_{(A,B,\varphi)} |1 - U_n/U_m|, \tag{19}$$

where U_n denotes a specific nth order spectral approximation of the function U. The maximum is typically evaluated over a regular grid of 6^3 points. We take $n_A = n_B = 2n_\varphi = n$, with the only exception $n_\varphi = 4$ which we use in axisymmetric situations.

Choosing a large value m defines a reference solution to which solutions at a lower order of approximation $n < m$ can be compared. This method gives a reliable characterization of convergence in our examples. Furthermore, we reduce the error in the solution of the discrete nonlinear system (13) below the error due to the finite order of the spectral approximation which therefore dominates the accuracy of the method.

The convergence rate of a spectral method is called *exponential* if the logarithm of the total error of an approximate solution depends linearly on the corresponding approximation order for sufficiently large order. This behavior is usually encountered if the underlying solution to be approximated is analytic everywhere on the spectral domain. However, if the solution is only C^k differentiable, the logarithm of the total error depends linearly on the logarithm of the approximation order. In particular, the slope of this line is $(k + 2)$, and the scheme is called *algebraically* convergent to $(k + 2)$th order. Hence, from the numerical convergence of the spectral method, one can deduce the differentiability of the solution to be approximated (see Figs. 1, 2, and 4 below for representative examples corresponding to puncture initial data).

III. PUNCTURE DATA

In the ADM formulation of a "3 + 1" splitting of the spacetime manifold, the vacuum Hamiltonian and the momentum constraint equations of general relativity read as follows:

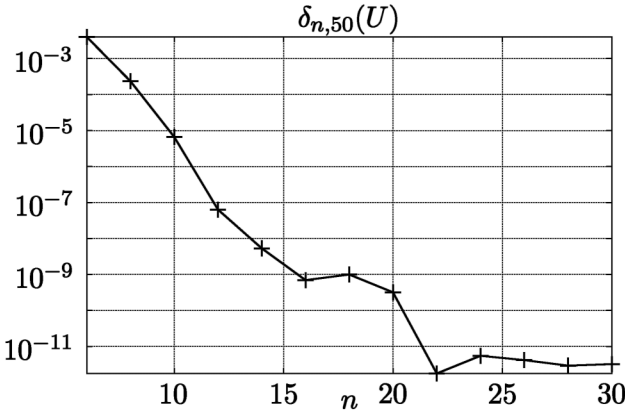

FIG. 1. For a single puncture with vanishing linear momentum parameter the spin $S^i = m^2 w \delta^i_1$ with $w = 0.2$ has been chosen. The plot shows the relative global accuracy of the spectral method for expansion order $n_A = n_B = n$ compared to a reference solution with $n = 50$ [see (19)]. For this axisymmetric example we have used $n_\varphi = 4$.

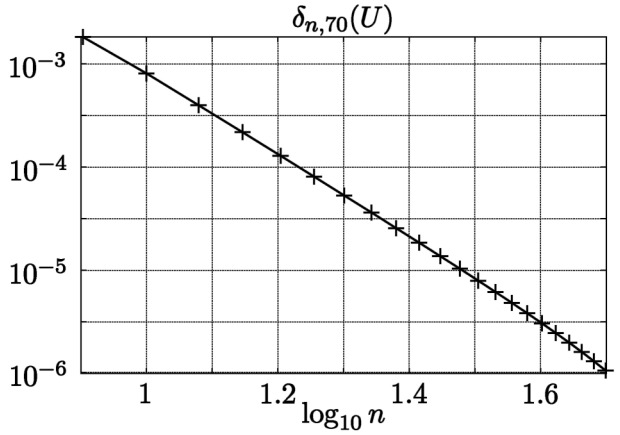

FIG. 2. For a single puncture with vanishing spin parameter the linear momentum $P^i = m\upsilon\delta^i_1$ with $\upsilon = 0.2$ has been chosen. The plot shows the relative global accuracy of the spectral method for expansion order $n_A = n_B = n$ compared to a reference solution with $n = 70$ [see (19)]. For this axisymmetric example we have used $n_\varphi = 4$.

$$R^2 + K^2 - K_{ij}K^{ij} = 0, \tag{20}$$

$$\nabla(K^{ij} - \gamma^{ij}K) = 0. \tag{21}$$

Here γ_{ij} is the 3-metric, K_{ij} the extrinsic curvature, K its trace, and R, ∇ are the Ricci scalar and the covariant derivative, respectively, associated with γ_{ij}.

Following York's conformal-transverse-traceless decomposition method [1], we make the following assumptions for the metric and the extrinsic curvature (δ_{ij} denotes the three-dimensional Kronecker symbol):

$$\gamma_{ij} = \psi^4\delta_{ij}, \tag{22}$$

$$K_{ij} = \psi^{-2}(V_{j,i} + V_{i,j} - \tfrac{2}{3}\delta_{ij}\mathrm{div}\,\boldsymbol{V}). \tag{23}$$

The initial data described by this method are conformally flat and maximally sliced, $K = 0$. With this ansatz the Hamiltonian constraint yields an equation for the conformal factor ψ,

$$\triangle\psi + \tfrac{1}{8}\psi^5 K_{ij}K^{ij} = 0, \tag{24}$$

while the momentum constraint yields an equation for the vector potential $\boldsymbol{V}$,

$$\triangle\boldsymbol{V} + \tfrac{1}{3}\mathrm{grad}(\mathrm{div}\,\boldsymbol{V}) = 0. \tag{25}$$

One can proceed by choosing a nontrivial analytic solution of the Bowen-York type for the momentum constraint,

$$\boldsymbol{V} = \sum_{n=1}^{N_p}\left(-\frac{7}{4|\boldsymbol{x}_n|}\boldsymbol{P}_n - \frac{\boldsymbol{x}_n\cdot\boldsymbol{P}_n}{4|\boldsymbol{x}_n|^3}\boldsymbol{x}_n + \frac{1}{|\boldsymbol{x}_n|^3}\boldsymbol{x}_n\times\boldsymbol{S}_n\right), \tag{26}$$

with poles at a finite number of N_p spatial points, the locations of the punctures. Here the vector parameters $\boldsymbol{P}_n$ and $\boldsymbol{S}_n$ can be identified with the physical linear and angular momenta of the nth puncture. The vector $\boldsymbol{x}_n$ points from the nth puncture to the point (x, y, z), $\boldsymbol{x}_n = (x - x_n, y - y_n, z - z_n)^T$, and $|\boldsymbol{x}_n|$ is its Euclidian norm.

In [3] it is pointed out that for the extrinsic curvature determined by (26) a particular solution of the Hamiltonian constraint is obtained by writing the conformal factor ψ as a sum of a singular term and a finite correction u,

$$\psi = 1 + \sum_{n=1}^{N_p}\frac{m_n}{2|\boldsymbol{x}_n|} + u, \tag{27}$$

with $u \to 0$ as $|\boldsymbol{x}_n| \to \infty$. The parameter m_n is called the bare mass of the nth puncture.

The main point of the puncture construction is that in terms of u the Hamiltonian constraint becomes a well-defined equation on the entire Cartesian 3-space (see [38] for a general existence theorem for such asymptotically flat initial data). However, it turns out that u is in general only C^2 at the punctures, although it is C^∞ elsewhere.

As discussed in Sec. II, such a drop of differentiability implies that a spectral method can only be expected to be algebraically convergent to fourth order. We first show for a single puncture that a simple coordinate transformation can resolve the differentiability problem at the location of the punctures. After that we discuss similar techniques for two punctures.

Note that by virtue of Theorem 1 by Dain and Friedrich [38], the conformal factor can only be expected to be globally C^∞ differentiable with respect to our coordinates (A, B, φ) if the individual linear momenta $\boldsymbol{P}_n$ vanish. In fact, we will find that for punctures with linear momenta the conformal factor possesses logarithmic terms when expanded at infinity, i.e., at $A = 1$. This holds also true if the total linear momentum, i.e., the sum of all $\boldsymbol{P}_n$ vanishes. Consequently, our single-domain spectral method cannot be exponentially convergent. Nevertheless, the scheme is rapidly converging towards highly accurate numerical solutions.

IV. SINGLE-PUNCTURE INITIAL DATA

For a single puncture at the origin of a Cartesian grid, we introduce spherical coordinates (r, ϑ, φ) via

$$x = r\cos\vartheta, \qquad y = r\sin\vartheta\cos\varphi, \qquad z = r\sin\vartheta\sin\varphi, \tag{28}$$

where

$$r \in [0, \infty), \qquad \vartheta \in [0, \pi], \qquad \varphi \in [0, 2\pi). \tag{29}$$

The conformal factor for a single puncture is

$$\psi = 1 + \frac{m}{2r} + u, \tag{30}$$

and we therefore choose to compactify the spatial domain by introducing a new radial coordinate A by

$$A = \left(1 + \frac{m}{2r}\right)^{-1}, \tag{31}$$

which implies (4).

We separately investigate the two situations in which either the linear momentum $\boldsymbol{P}$ or the spin $\boldsymbol{S}$ vanishes. A single black hole with either small Bowen-York spin or linear momentum has also been considered in [39–41].

A. Single puncture with spin

Consider first a single puncture with $\boldsymbol{P} = 0$ and $S^i = S_x \delta^i_1$. In the chosen spherical coordinates the Hamiltonian constraint reads

$$\triangle\psi + \frac{9S_x^2}{16r^6}\psi^{-7}\sin^2\vartheta = 0. \tag{32}$$

For the auxiliary function u we obtain a nonlinear Poisson-like equation,

$$u_{AA} + \frac{2u_A}{A} + \frac{1}{A^2(1-A)^2}\left(u_{\vartheta\vartheta} + u_\vartheta \cot\vartheta + \frac{u_{\varphi\varphi}}{\sin^2\vartheta}\right) = -\frac{36w^2A(1-A)^2}{(1+Au)^7}\sin^2\vartheta \tag{33}$$

with $w = S_x/m^2$. The solution u is uniquely determined by regularity and periodicity conditions at $\vartheta = 0$, $\vartheta = \pi$ and $\varphi = 0$, $\varphi = 2\pi$, respectively. For $A = 0$ only a regularity condition needs to be imposed, while for $A = 1$ we set $u = 0$. Thus, the single-domain spectral method described in Sec. II is applicable with

$$B = 2\vartheta/\pi - 1, \tag{34}$$

provided that a global regular solution exists.

In order to study the behavior of u globally, and, in particular, close to the puncture, consider the following Taylor series which converges for sufficiently small w:

$$u = \sum_{j=1}^{\infty} w^{2j} u_j. \tag{35}$$

All u_j can explicitly be given in closed analytic form. In particular, for u_1 we obtain (P_2 denotes the second Legendre polynomial):

$$u_1 = u_{1,0} + u_{1,2}P_2(\cos\vartheta), \tag{36}$$

$$u_{1,0} = \tfrac{2}{5}(-2A^5 + 6A^4 - 5A^3 + 1), \tag{37}$$

$$u_{1,2} = \tfrac{4}{5}(1-A)^3A^2. \tag{38}$$

Note that u_1 is regular at $A = 0$ in the spherical coordinates (A, ϑ, φ). The same holds for all u_j and in fact for u (see [38]). Hence, the C^2 differentiability of u at the puncture has been translated into a C^∞ differentiability with respect to spherical coordinates. We can still recognize the original behavior of the function which is exhibited by the fact that u_1 possesses a term $\sim r^3$ which is C^2 differentiable in Cartesian coordinates. However, in the chosen spherical coordinates (A, ϑ, φ), u becomes globally C^∞.

Consequently, the application of our single-domain spectral method exhibits exponential convergence, which can be seen in Fig. 1 for a representative example.

B. Single puncture with linear momentum

Consider now a single puncture with linear momentum $P^i = P_x\delta^i_1$ and vanishing spin. The Hamiltonian constraint becomes

$$\triangle\psi + \frac{9P_x^2}{16r^4}\psi^{-7}(1 + 2\cos^2\vartheta) = 0. \tag{39}$$

Similar to the treatment in the previous section we obtain in spherical coordinates the nonlinear Poisson-like equation

$$u_{AA} + \frac{2u_A}{A} + \frac{1}{A^2(1-A)^2}\left(u_{\vartheta\vartheta} + u_\vartheta\cot\vartheta + \frac{u_{\varphi\varphi}}{\sin^2\vartheta}\right) = -\frac{9v^2A^3}{4(1+Au)^7}(1 + 2\cos^2\vartheta) \tag{40}$$

with $v = P_x/m$. Again, we may study the behavior of u by performing a Taylor expansion which converges for sufficiently small v,

$$u = \sum_{j=1}^{\infty} v^{2j}u_j. \tag{41}$$

All u_j can explicitly be given in closed analytic form. In particular, for u_1 we obtain

$$u_1 = u_{1,0} + u_{1,2}P_2(\cos\vartheta), \tag{42}$$

$$u_{1,0} = \tfrac{1}{8}(1 - A^5), \tag{43}$$

$$u_{1,2} = \frac{(1-A)^2}{20A^3}[84(1-A)\log(1-A) + 84A - 42A^2 - 14A^3 - 7A^4 - 4A^5 - 2A^6]. \tag{44}$$

We recover that u is analytic at $A = 0$ while it is C^4 differentiable in Cartesian coordinates, which is implied by a term $\sim r^5$.

However, the solution $u = u(A, \vartheta, \varphi)$ also possesses logarithmic terms with a branch point at $A = 1$ ($r \to \infty$). For a single puncture, such logarithmic terms are known to occur for nonvanishing linear momentum, e.g., [38,40]. In particular, the leading term

$$\frac{21(1-A)^3}{5A^3}\log(1-A) \tag{45}$$

gives rise to a mere C^2 differentiability of u at $A = 1$.

This fact again is reflected by the spectral method, which now converges only algebraically to fourth order as expected; see Fig. 2 for a representative example.

V. TWO-PUNCTURE INITIAL DATA

Consider two punctures that are placed symmetrically on the x axis at $x = \pm b$ so that $D = 2b$ is the distance between the two punctures. We denote the bare mass of the punctures by $m_\pm$, the linear momenta by $\mathbf{P}_\pm$ and the spin parameters by $\mathbf{S}_\pm$; the subscripts refer to the corresponding locations at $x = \pm b$.

In the following we introduce appropriate coordinates in which the auxiliary function u becomes regular at the location of the punctures.

The decomposition (27) reads

$$\psi = 1 + \frac{m_+}{2r_+} + \frac{m_-}{2r_-} + u, \tag{46}$$

with the distances from the punctures given by

$$r_\pm = \sqrt{(x \mp b)^2 + y^2 + z^2}. \tag{47}$$

As we have seen for the single-puncture initial data problem, the auxiliary function u discussed there is regular at the location of the puncture in spherical coordinates about this point. We therefore expect a similar regular behavior if we were to introduce coordinates that become spherical at both punctures. However, regularity of u at the punctures can also be achieved if we use specific coordinates in which the distances $r_\pm$ are analytic functions there (see [38]). This is a weaker condition because it does not necessarily require one of our coordinates to behave as $r_\pm$ close to the punctures.

A coordinate transformation that describes this situation at the origin in two dimensions is given by

$$c = C^2, \tag{48}$$

where

$$c = x + \mathrm{i}y \quad \text{and} \quad C = X + \mathrm{i}Y \tag{49}$$

are complex combinations of Cartesian coordinates (x, y) and new coordinates (X, Y). Clearly, the distance becomes regular with respect to X and Y,

$$\sqrt{x^2 + y^2} = \sqrt{c\bar{c}} = C\bar{C} = X^2 + Y^2. \tag{50}$$

Note that transformation (48) maps a right angle at the origin to a straight line through the origin.

For the two-puncture initial data problem, we apply this idea by introducing a specific mapping

$$(A, B, \varphi) \mapsto (x, y, z), \tag{51}$$

which is composed of several transformations (see Fig. 3),

$$(A, B, \varphi) \mapsto (\xi, \eta, \varphi) \mapsto (X, R, \varphi) \mapsto (x, \rho, \varphi) \mapsto (x, y, z). \tag{52}$$

These transformations are chosen to realize the two different aspects of the desired entire transformation: (i) regularity of $r_\pm$ at both punctures and (ii) mapping of a compact rectangular domain in $\mathbb{R}^3$ to the entire space of (x, y, z) coordinates.

We first introduce cylindrical coordinates (x, ρ, φ) such that

$$y = \rho\cos\varphi, \qquad z = \rho\sin\varphi, \qquad \varphi \in [0, 2\pi), \tag{53}$$

and combine x and ρ to form c,

$$c = x + \mathrm{i}\rho. \tag{54}$$

Now consider the transformation

$$c = \frac{b}{2}(C + C^{-1}), \qquad \text{where } C = X + \mathrm{i}R. \tag{55}$$

It maps the region of the upper half plane with coordinates (X, R) which is exterior to the unit circle onto the upper half plane of our coordinates (x, ρ) [see Figs. 3(c) and 3(d)].

The key motivation behind this transformation has been to produce locally at each puncture the same effect on angles as has been done above in the transformation (48) and (49) and which has resulted in the regular expression (50) for the distance from the origin. Similarly we now obtain expressions for the distances from either puncture

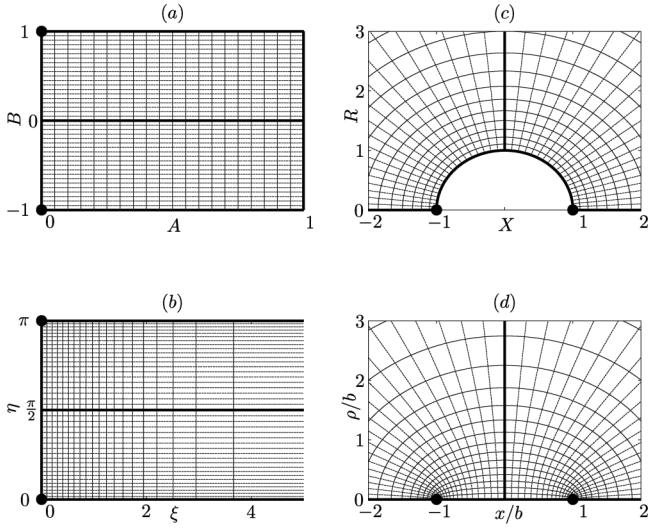

FIG. 3. Several coordinate patches for the two-puncture initial data problem. Shown are (a) equidistant coordinate lines in the system of spectral coordinates (A, B), as well as (b) their images in prolate spheroidal coordinates (ξ, η), (c) in the coordinates (X, R), and (d) in cylindrical coordinates (x, ρ). The punctures are indicated by bullets. The $x = 0$ plane, several sections of the x axis and their corresponding images in the other coordinate systems, as well as spatial infinity given by $A = 1$ are emphasized by thick lines.

$$r_{\pm} = |c \mp b| = \frac{b}{2\sqrt{X^2 + R^2}}[(X \mp 1)^2 + R^2] \qquad (56)$$

which are regular with respect to X and R at the punctures, i.e., at $c = \pm b$ or $C = \pm 1$.

Next we need to find a transformation which maps a compact rectangular region onto the region of (X, R) coordinates. As a first step, the polar transformation

$$C = e^{\zeta}, \qquad \zeta = \xi + i\eta, \qquad \xi \in [0, \infty), \eta \in [0, \pi] \qquad (57)$$

yields a strip which is infinitely extended with respect to positive ξ values [see Fig. 3(b)]. Writing c in terms of ζ gives

$$c = b \cosh\zeta. \qquad (58)$$

Thus we recover the transformation

$$x = b \cosh\xi \cos\eta, \qquad \rho = b \sinh\xi \sin\eta, \qquad (59)$$

which maps the well-known prolate spheroidal coordinates (ξ, η) onto cylindrical coordinates. Hence, constant ξ and η values correspond to confocal ellipses and hyperbolas, respectively, in the (x, ρ) plane. Their focal points are located at the two punctures, i.e., at $(\xi, \eta) = (0, 0)$ and $(\xi, \eta) = (0, \pi)$ (see Fig. 3). The distances $r_{\pm}$ expressed in terms of ξ and η are

$$r_{\pm} = b(\cosh\xi \mp \cos\eta). \qquad (60)$$

For a compactification we choose the relations

$$\xi = 2 \operatorname{artanh} A, \qquad \eta = \frac{\pi}{2} + 2 \arctan B. \qquad (61)$$

In summary, the transformation from (A, B, φ) to (x, y, z) takes the (somewhat symmetric) form

$$x = b\frac{A^2 + 1}{A^2 - 1}\frac{2B}{1 + B^2}, \qquad y = b\frac{2A}{1 - A^2}\frac{1 - B^2}{1 + B^2}\cos\varphi,$$
$$z = b\frac{2A}{1 - A^2}\frac{1 - B^2}{1 + B^2}\sin\varphi. \qquad (62)$$

It is now straightforward to apply our single-domain spectral method to solve the Hamiltonian constraint (24) for the two-puncture initial data problem. Again we impose $u \to 0$ as $A \to 1$, i.e., $(x^2 + y^2 + z^2) \to \infty$. As in the one-puncture initial data problem, at all the other boundaries we again merely require regularity of the solution which replaces a particular boundary condition there. As expected, the auxiliary function u is C^{∞} at the two punctures.

As mentioned at the end of Sec. III, in general u possesses logarithmic terms when expanded at infinity, $A = 1$. In [38] a theorem is proved that does not exclude the existence of such logarithmic terms given the falloff condition satisfied by the extrinsic curvature that we consider here. We have checked in the case of axisymmetry analytically that for two equal mass punctures with linear momentum logarithmic terms do indeed occur. The only exception is when both linear momenta $\boldsymbol{P}_{\pm}$ vanish, in which case the solution is also C^{∞} at $A = 1$. Otherwise we obtain terms $\sim(1 - A)^3 \log(1 - A)$ if the total momentum $\boldsymbol{P} = \boldsymbol{P}_{+} + \boldsymbol{P}_{-} \neq 0$, and terms $\sim(1 - A)^5 \log(1 - A)$ if $\boldsymbol{P} = 0$. In other words, in the center of mass frame where the total linear momentum vanishes the leading order logarithmic terms cancel, but next to leading order logarithmic terms are still present such that the solution is only C^4 at $A = 1$. Although we carried out this analysis for axisymmetry, it is to be expected that the same result applies to puncture data describing orbiting black holes in the center of mass frame.

A representative convergence rate of our single-domain spectral method is displayed in Fig. 4. We show the relative accuracy (19), which involves the maximum over a set of points, computed over a 3D set of points as before, but also for points only at infinity and at the puncture. The error is dominated by errors near the puncture down to about 10^{-9} for $n < 35$. In this regime convergence of the maximal error is exponential. However, the error at infinity only converges algebraically at roughly sixth order as expected. Around $n = 35$, the error at infinity overtakes the error elsewhere and the overall convergence becomes algebraic.

Therefore we conclude that our numerical method is successful since it obtains exponential convergence for orbiting punctures down to about 10^{-9} with relatively

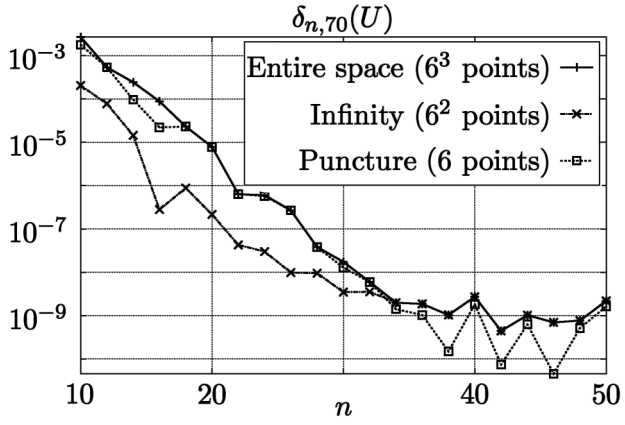

FIG. 4. Two punctures with vanishing spins. The physical parameters are given by $m_{+} = m_{-} = b, P^i_{\pm} = \pm 0.2 b \delta^i_2$. For this plot we took $n_A = n_B = 2n_{\varphi} = n$ and compared to a reference solution with $n = 70$. Apart from the global relative accuracy [see (19)] taken over 6^3 spatial points, the corresponding maximal deviations at infinity and at the punctures are shown. For small n, the error near the punctures is about 10 times larger than the error at infinity, and the convergence rate is approximately exponential down to about 10^{-9}. The error at infinity converges at roughly sixth algebraic order as expected, and for sufficiently large n this becomes the dominant convergence rate.

small computational resources. At the punctures our coordinate transformation leads to a smooth solution, but at infinity there are logarithmic terms which lead to algebraic convergence of sixth order. We consider this quite satisfactory since higher accuracy is rarely needed in numerical relativity. In principle, it should be possible to eliminate the leading logarithmic term which should bring the calculation close to numerical round-off errors. However, it is unclear whether logarithmic terms can be avoided completely in this approach, for example, by an appropriate coordinate transformation.

In Fig. 5 we compare the result for u obtained by the spectral method with u computed by the second order finite difference multigrid method on a fixed mesh refinement implemented in BAM previously [3,15]. As an example we picked the parameters $b = 3M$, $m_+ = m_- = 0.5M$, and $P^i_+ = -P^i_- = 0.2M\delta^i_2$. The ADM linear momentum at infinity vanishes. For the purpose of this discussion we have defined $M = m_+ + m_-$. For these parameters we can restrict the computational domain to one quadrant of a Cartesian box centered at the origin. We computed the multigrid data at three overall resolutions using seven levels of refinement with approximately the same geometrical layout of the boxes. The highest resolution was obtained for $98 \times 98 \times 50$ points on the finest level, while to test convergence we successively doubled the grid spacing, resulting in a grid spacing of $M/64$, $M/32$, and $M/16$ on the finest level. The face of the outermost box is located at about $48M$ in each case.

The main result is that the two methods verify each other quite accurately on this scale near the punctures and also for large x. Near the punctures it is a question of resolution whether the known feature of a local indentation is fully resolved. For the chosen parameters both methods reach this level of resolution, but the spectral method uses significantly less resources.

VI. TWO PUNCTURES IN THE TEST MASS LIMIT

Apart from the high accuracy that can be achieved by spectral methods, they also prove to be very useful for the investigation of critical and limiting situations. For the binary black hole initial data problem, a situation of this kind is encountered when the two gravitational sources possess very different masses. It is the aim of this section to apply our spectral method for the binary-puncture initial data problem in this limiting case.

As a first step we perform the test mass limit analytically. The results arising from this study will then be compared to those obtained by the spectral method for a small mass ratio.

We consider two nonspinning punctures with bare masses m_- and m_+ located on the y axis at $y = 0$ and

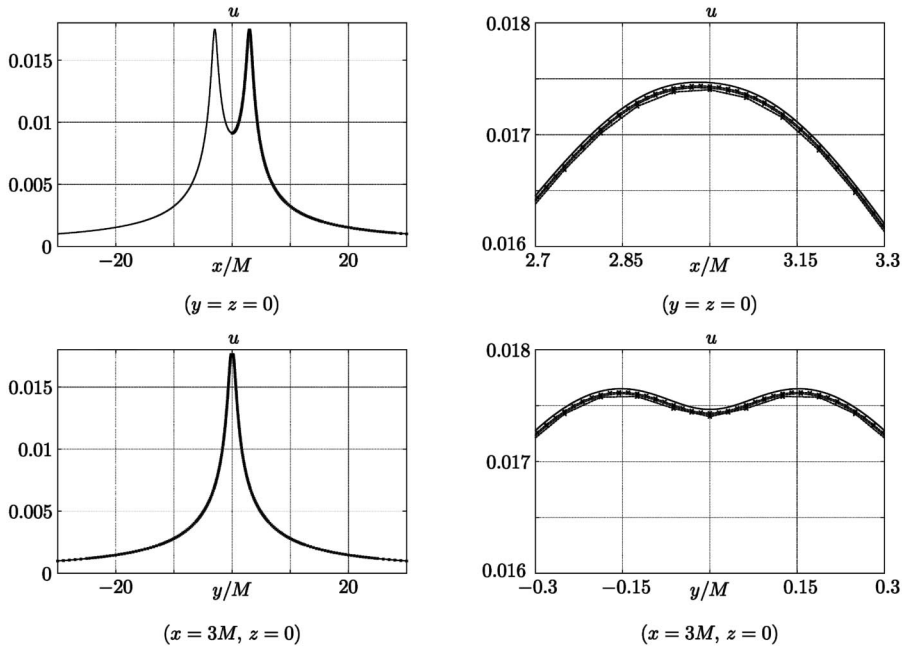

FIG. 5. Example for a solution to the Hamiltonian constraint obtained with the spectral method and with a multigrid method on nested Cartesian grids. Shown is the regular part u of the conformal factor for two punctures without spin and vanishing total linear momentum, which are located on the x axis at $x = \pm 3M$. Results from the multigrid method are indicated by lines with markers. The panels on the left show the various levels of refinement combined into one line for the highest resolution (see text). The panels on the right show an enlargement of the region near one of the punctures for three resolutions of the multigrid method. In all panels the result for the single-domain spectral method with $n_A = n_B = 40$ and $n_\varphi = 20$ is shown as a solid line without markers. Note that on this scale the methods agree well both far away and close to the punctures.

$y = D$, respectively, and perform the test mass limit by choosing $m_- \to 0$ with D and m_+ held fixed. We moreover assume that the linear momenta are given by (v_- and $\hat{P}^i_+$ fixed, $v_- \neq 0$)

$$P^i_- = m_- v_- \delta^i_1, \qquad P^i_+ = m_- \hat{P}^i_+, \tag{63}$$

which implies that the total linear momentum vanishes as $m_- \to 0$. Thus, in this limit we will have placed ourselves in a frame in which the total linear momentum vanishes.

In order to understand the behavior of u in the entire spatial domain, we have to consider two different ways of performing this limit separately:

(1) If we calculate the auxiliary function u at a given spatial point at some finite distance from the origin, i.e., at *fixed* coordinates $(x, y, z) \neq (0, 0, 0)$, we will find that u tends to zero in this limit. In particular,

$$\lim_{m_- \to 0}\left(\frac{u}{m_-}\right) = \frac{\Delta\mu_\infty}{2r}, \tag{64}$$

where $r = \sqrt{x^2 + y^2 + z^2}$. The physical meaning of the constant $\Delta\mu_\infty$ (which is obtained through the second limiting process, see below) with respect to the system's relative binding energy in this limit will be discussed in Sec. VII.

(2) If, on the contrary, we hold the *relative* coordinates $(\tilde{x}, \tilde{y}, \tilde{z}) = (x/m_-, y/m_-, z/m_-)$ fixed, we maintain finite values for u at these spatial points. In particular, the resulting u obeys a constraint equation valid for a modified single-puncture initial data problem with nonvanishing linear momentum $\boldsymbol{P}$ (and no spin). The above constant $\Delta\mu_\infty$ can be read off from these data.

For both ways of establishing the test mass limit, we rewrite the Hamiltonian constraint as an integral equation,

$$u(\boldsymbol{x}) = \frac{1}{32\pi}\int_{\mathbb{R}^3} \frac{\psi^5 K_{ij}K^{ij}}{|\boldsymbol{x} - \boldsymbol{x}'|}\, d^3\boldsymbol{x}'. \tag{65}$$

Introducing spherical coordinates

$$x = r\cos\vartheta, \qquad y = r\sin\vartheta\cos\varphi, \qquad z = r\sin\vartheta\sin\varphi, \tag{66}$$

this integral equation becomes

$$\begin{aligned} u(r,\vartheta,\varphi) = \frac{m_-^2 v_-^2}{32\pi}\int_0^{2\pi} d\varphi' \int_0^{\pi} \sin\vartheta' d\vartheta' \int_0^{\infty} \frac{r'^2 dr'}{|\boldsymbol{x} - \boldsymbol{x}'|} \\ \times\left\{\left(1 + \frac{m_+}{2r_+} + \frac{m_-}{2r'} + u\right)^{-7}\left[\frac{9}{2r'^4}(1 + 2\cos^2\vartheta') \right.\right. \\ \left.\left. + \frac{g}{r'^2 r_+^2} + \frac{h}{r_+^4}\right]\right\}, \end{aligned} \tag{67}$$

where $\boldsymbol{x}' = (x', y', z')^T$ with

$$\begin{aligned} x' &= r'\sin\vartheta', \qquad y' = r'\cos\vartheta'\cos\varphi', \\ z' &= r'\cos\vartheta'\sin\varphi', \end{aligned} \tag{68}$$

and

$$r_+ = \sqrt{x'^2 + (y' - D)^2 + z'^2}. \tag{69}$$

The functions g and h depend on $\hat{P}^i_+$, v_- and D. They remain finite everywhere.

We now perform the two different limits.

1. Consider fixed values $r > 0$. We split the integration with respect to r' such that (a) $r' \in [r/2, \infty)$ and (b) $r' \in [0, r/2]$.

For (a) observe that for $r' \geq r/2$ the term

$$\left\{\left(1 + \frac{m_+}{2r_+} + \frac{m_-}{2r'} + u\right)^{-7}\left[\frac{9}{2r'^4}(1 + 2\cos^2\vartheta') + \frac{g}{r'^2 r_+^2} + \frac{h}{r_+^4}\right]\right\}$$

remains regular in the limit $m_- \to 0$, and thus, the contribution of the corresponding Poisson integral, evaluated for $r' \in [r/2, \infty)$, is of order $\mathcal{O}(m_-^2)$.

Performing for the remaining near-zone integral (b) the substitution $r' = m_- s'$ leads us to

$$\begin{aligned} &\frac{18 m_- v_-^2}{\pi r}\int_0^{2\pi} d\varphi' \int_0^{\pi} \sin\vartheta' d\vartheta' \int_0^{r/(2m_-)} \\ &\times ds'\left(s'^5 \frac{1 + 2\cos^2\vartheta' + \mathcal{O}(s' m_-)}{\{1 + 2s'[1 + m_+/(2D) + u]\}^7}\right), \end{aligned}$$

from which it follows that

$$\lim_{m_- \to 0} \frac{u(r,\vartheta,\varphi)}{m_-} = \frac{\Delta\mu_\infty}{2r} \tag{70}$$

with the constant $\Delta\mu_\infty$ given by

$$\Delta\mu_\infty = \frac{36 v_-^2}{\pi}\left\{ \begin{array}{l} \int_0^{2\pi} d\varphi \int_0^{\pi} \sin\vartheta(1 + 2\cos^2\vartheta) d\vartheta \int_0^{\infty} ds \times \\ s^5\{1 + 2s[1 + m_+/(2D) + \tilde{u}]\}^{-7}. \end{array}\right. \tag{71}$$

Here, the function $\tilde{u}$ is defined by

$$\tilde{u}(s,\vartheta,\varphi) = \lim_{m_- \to 0} u(m_- s,\vartheta,\varphi), \tag{72}$$

and turns out to be the auxiliary potential resulting from the second limit, which we will discuss now.

2. Take for the fixed relative distance limit $r = m_- s$ with s fixed, $s \geq 0$, for which we may perform the analogous steps as in the previous case. We calculate the first integral for $r' \in [D/2, \infty)$, and again get only a contribution of order $\mathcal{O}(m_-^2)$. For the near-zone integral we obtain

$$\begin{aligned} &\frac{18 v_-^2}{\pi}\int_0^{2\pi} d\varphi' \int_0^{\pi} \sin\vartheta'\, d\vartheta' \int_0^{D/(2m_-)} \frac{ds'}{|\tilde{\boldsymbol{x}} - \tilde{\boldsymbol{x}}'|} \\ &\times\left(s'^5 \frac{1 + 2\cos^2\vartheta' + \mathcal{O}(s' m_-)}{\{1 + 2s'[1 + m_+/(2D) + u]\}^7}\right) \end{aligned}$$

with vectors

$$\tilde{\boldsymbol{x}} = (\tilde{x}, \tilde{y}, \tilde{z})^T = \boldsymbol{x}/m_-, \qquad \boldsymbol{x}' = (\tilde{x}', \tilde{y}', \tilde{z}')^T = \boldsymbol{x}'/m_-,$$

where

$$\tilde{x} = s\sin\vartheta, \qquad \tilde{x}' = s'\sin\vartheta', \qquad \tilde{y} = s\cos\vartheta\cos\varphi,$$
$$\tilde{y}' = s'\cos\vartheta'\cos\varphi', \qquad \tilde{z} = s\cos\vartheta\sin\varphi,$$
$$\tilde{z}' = s'\cos\vartheta'\sin\varphi'.$$

This leads in the limit $m_- \to 0$ to an integral equation for the function $\tilde{u}$ introduced above. Equivalently, we may consider the corresponding differential equation

$$\triangle\tilde{u} + \frac{9v_-^2}{16s^4}\tilde{\psi}^{-7}(1 + 2\cos^2\vartheta) = 0 \tag{73}$$

with

$$\tilde{\psi} = 1 + \frac{m_+}{2D} + \frac{1}{2s} + \tilde{u}, \tag{74}$$

and the Laplace operator taken in the spherical coordinates (s, ϑ, φ). In particular it follows that

$$\lim_{s\to\infty} 2s\tilde{u}(s, \vartheta, \varphi) = \Delta\mu_\infty. \tag{75}$$

We moreover see that for the function

$$\hat{u} = \hat{m}\,\tilde{u} \qquad \text{with } \hat{m} = \left(1 + \frac{m_+}{2D}\right)^{-1} \tag{76}$$

we recover the equation valid for a single-puncture initial data problem (without spin) (see Sec. IV B). The (dimensionless) bare mass is just $\hat{m}$, and the corresponding momentum reads

$$\pi_x = v_-\hat{m}^4. \tag{77}$$

The above analytic study shows that we can use our spectral methods applied to a single puncture with nonvanishing momentum (as described in Sec. IV B) in order to evaluate the test mass limit with algebraic convergence of fourth order. These results can be compared with the values obtained for a corresponding two-puncture initial data problem with a small mass ratio (see Table I). In this table, one finds the value $u_- = u(0, 0, 0)$ at the origin (i.e., at the "light" puncture), the expression

$$\frac{2D}{m_-}u_+ = \frac{2D}{m_-}u(0, D, 0) \tag{78}$$

(i.e., at the "heavy" puncture), and the limit

$$\lim_{r\to\infty}\left(\frac{2ru}{m_-}\right), \tag{79}$$

where the latter two tend to $\Delta\mu_\infty$ as $m_- \to 0$. We have chosen a particular example where the distance D and the velocity v_- obey the relations valid for the last stable circular orbit of a test particle in the gravitational field of a Schwarzschild black hole of mass m_+:

TABLE I. Test mass limit $m_- \to 0$ for the representative example with values given in (80) with $P_-^i = -P_+^i = -m_- v_- \delta_1^i$. For the above nonvanishing mass ratios we used the spectral method for the binary-puncture initial data problem with $n_A = n_B = 2n_\varphi = 100$. The last line has been calculated with the spectral method for the single-puncture initial data problem with $n_A = n_B = 70$, $n_\varphi = 4$.

m_-/m_+	u_-	$2Du_+/m_-$	$\lim_{r\to\infty}(2ru/m_-)$
10^{-1}	0.034 17	0.2011	0.1688
10^{-2}	0.034 06	0.1635	0.1601
10^{-3}	0.034 06	0.1596	0.1592
0	0.034 056 8	0.159 094	0.159 094

$$\frac{D}{m_+} = \frac{5}{2} + \sqrt{6}, \qquad v_- = \frac{4\sqrt{3}}{5 + 2\sqrt{6}}. \tag{80}$$

Moreover, we simply set $\hat{P}_+^i = -v_-\delta_1^i$.

It turns out that for ratios $m_-/m_+ \geq 10^{-3}$ the spectral scheme yields reliable results that approach those of the test mass limit. For mass ratios of 10^{-3}, four digits of accuracy are obtained for the given order of approximation from the two-puncture calculation, while six digits are obtained with the single-puncture method for the test mass limit.

VII. BINDING ENERGY IN THE TEST MASS LIMIT

In this section we use the results of the previous section to compute the binding energy of two punctures without spin in the limit of vanishing mass ratio. The aim will be to compare the binding energy in this test mass limit with the binding energy of a test particle in Schwarzschild spacetime. The deviation of the puncture binding energy from the Schwarzschild result will yield a quantitative statement about how realistic puncture data are in this limit. If punctures were completely realistic we should recover the Schwarzschild results. A related study of small mass ratios (up to 1/32) has already been performed by Pfeiffer [42] for excision-type initial data with Bowen-York extrinsic curvature, and also to a limited extent for conformal thin sandwich initial data.

In order to define a binding energy we need a notion of the total mass as well as of the local black hole masses. The ADM mass at infinity yields a well-defined global mass. For two punctures it is given by

$$M_\infty^{\mathrm{ADM}} = m_+ + m_- + \Delta M_\infty, \tag{81}$$

where

$$\Delta M_\infty = -\frac{1}{2\pi}\oint_\infty \nabla_i u\, dA^i = \lim_{r\to\infty} 2ru. \tag{82}$$

On the other hand, it is impossible to unambiguously define local black hole masses in general. In the following we choose the ADM mass

$$M_{\pm}^{\rm ADM} = (1 + u_{\pm})m_{\pm} + \frac{m_+ m_-}{2D} \tag{83}$$

computed in the asymptotically flat region at each puncture as a measure of the local black hole mass [6]. Here u_+ and u_- are the values of u at each puncture. As shown by Beig [26], this definition of local mass has the following advantage. For a single slowly moving puncture with momentum $\boldsymbol{P}_{\infty}^{\rm ADM} = \boldsymbol{P}_-$, the ADM energy $E_{\infty}^{\rm ADM}$ at infinity is related to the ADM mass $M_-^{\rm ADM}$ as measured in the asymptotically flat region near the puncture by

$$E_{\infty}^{\rm ADM} = M_-^{\rm ADM} + \frac{(\boldsymbol{P}_{\infty}^{\rm ADM})^2}{2M_-^{\rm ADM}} + O[(\boldsymbol{P}_{\infty}^{\rm ADM})^4], \tag{84}$$

which is just what one expects if the local mass definition is reasonable. If, for example, one uses instead the bare mass m_- as the definition of local mass, one finds (e.g., [26,43])

$$E_{\infty}^{\rm ADM} = m_- + \frac{5}{8}\frac{(\boldsymbol{P}_{\infty}^{\rm ADM})^2}{m_-} + O[(\boldsymbol{P}_{\infty}^{\rm ADM})^4], \tag{85}$$

which is incompatible with special relativity.

Next, we define the binding energy for two punctures by

$$\begin{aligned} E_b &= M_{\infty}^{ADM} - M_+^{ADM} - M_-^{ADM} \\ &= \Delta M_{\infty} - m_+ u_+ - m_- u_- - \frac{m_+ m_-}{D}. \end{aligned} \tag{86}$$

In the test mass limit of $m_- \to 0$, it follows from Eq. (64) that

$$\lim_{m_- \to 0} \Delta M_{\infty}/m_- = \Delta\mu_{\infty} \tag{87}$$

and

$$\lim_{m_- \to 0} u_+ = 0. \tag{88}$$

Thus E_b goes to zero in this limit. We therefore consider E_b/μ, where

$$\mu = M_+^{\rm ADM} M_-^{\rm ADM}/(M_+^{\rm ADM} + M_-^{\rm ADM}) \tag{89}$$

is the reduced mass. With the help of Eqs. (64), (75), (86), and (87), we find that

$$\begin{aligned} \lim_{m_- \to 0} \frac{E_b}{\mu} &= \lim_{m_- \to 0} E_b \left(\frac{1}{M_+^{\rm ADM}} + \frac{1}{M_-^{\rm ADM}} \right) \\ &= \frac{\Delta\mu_{\infty}(1 - \frac{m_+}{2D}) - u_- - \frac{m_+}{D}}{1 + u_- + \frac{m_+}{2D}}. \end{aligned} \tag{90}$$

This binding energy can now be compared with the binding energy of a test particle in Schwarzschild spacetime. For circular geodesics in Schwarzschild the binding energy, angular momentum, and angular velocity observed at infinity are given by

$$\frac{E_{b,S}}{\mu} = \frac{(2r - M)^2}{(2r + M)\sqrt{4r^2 - 8Mr + M^2}} - 1, \tag{91}$$

$$\frac{L_S}{\mu} = \frac{(2r + M)^2}{2r^2}\sqrt{\frac{Mr^3}{(4r^2 - 8Mr + M^2)}}, \tag{92}$$

and

$$\Omega_S = \sqrt{\frac{64Mr^3}{(2r + M)^6}}, \tag{93}$$

respectively, where M is the mass of the Schwarzschild black hole, μ is the mass of the test particle, and r is the orbital radius in isotropic coordinates.

In order to compute E_b/μ for punctures in the test mass limit we have to solve Eq. (73) with the appropriate velocity v_- for circular orbits. This raises two questions. The first is how to choose the coordinate distance D between the two punctures if one wants to compare with a test particle in Schwarzschild at isotropic radial coordinate r. The answer is that in the limit of $m_- \to 0$ the spacetime is determined by the puncture with bare mass m_+, so that one simply obtains Schwarzschild in isotropic coordinates, which allows us to set

$$D = r. \tag{94}$$

The second question is how one should choose v_- for two punctures in circular orbit. One could, for example, obtain v_- by requiring equality of Komar and ADM mass, which is a necessary condition for the existence of a helical Killing vector, as done in [13]. An alternative would be the effective potential method [8]. Each of these methods will give a binding energy and an angular momentum for the so-defined circular orbits and in general we do not expect the binding energy and angular momentum to exactly agree with the Schwarzschild results. For simplicity and in order to eliminate possible errors in the angular momentum we choose

$$v_- = \frac{L_S/\mu}{r} \tag{95}$$

so that the angular momentum of the light puncture exactly equals the angular momentum of a test particle in Schwarzschild spacetime.

Using our spectral method with $n_A = n_B = 70$ and $n_\varphi = 4$ we have computed the binding energy for punctures in the test mass limit. The result is plotted in Fig. 6 versus the angular velocity given in Eq. (93). Also shown are the results for circular orbits in Schwarzschild and several other binding energies in the equal mass case taken from [13,14]. One can see that the binding energy for punctures (solid line on bottom) in the test mass limit does not agree with the binding energy of a test particle in Schwarzschild (dotted line), except in the Newtonian limit of small $M\Omega$. The discrepancy reaches about 50% at the innermost stable circular orbit (ISCO) of Schwarzschild, which means that the amount of energy radiated before reaching the Schwarzschild ISCO is too large by 50% and that the location of the ISCO predicted

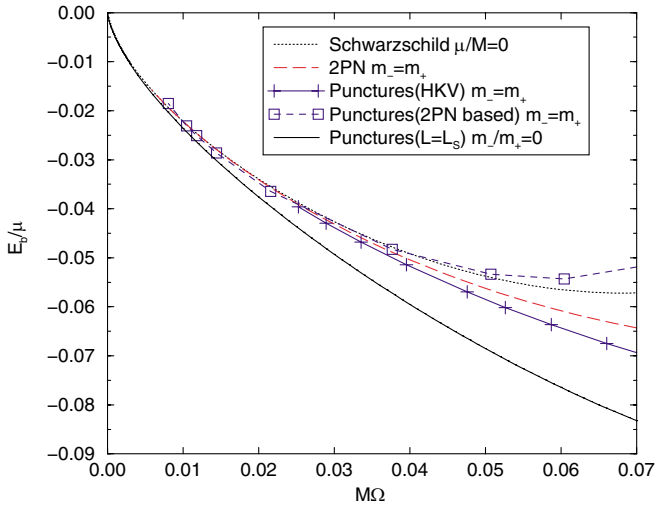

FIG. 6 (color online). The solid line on the bottom shows the binding energy versus angular velocity for two punctures in circular orbit in the test mass limit. For comparison we also show the binding energy of a test particle in Schwarzschild (dotted line). In addition we show several binding energies for circular orbits in the equal mass case. The post-2-Newtonian binding energy (broken line) is close to puncture data based on an approximate helical Killing vector (plusses) as well as to puncture data based on post-2-Newtonian data (squares), and also to the Schwarzschild result.

by puncture data is wrong. This means that, for the assumptions made in the definition of the binding energy, puncture data are not realistic for extreme mass ratios and that one cannot expect to obtain reliable predictions about the gravitational waves emitted.

Let us point out two possible reasons for the discrepancy. One is that it is not clear whether there are alternatives to our definition of mass, (83), that change the result. Another issue is that it is known that there is ''artificial'' radiation present in puncture data. Such radiation could contribute at the observed level to the ratio of infinitesimal binding energy to infinitesimal mass.

Interestingly, the curve for puncture data in Fig. 6 in the equal mass case (marked by pluses) is much closer to both the Schwarzschild (dotted line) case and the post-2-Newtonian (broken line) results, as well as to the results of the numerical method based on post-2-Newtonian data (marked by squares) discussed in [14]. This might indicate that artificial radiation affects the binding energy per reduced mass for comparable mass puncture data less than in the test mass limit.

Note also that in [44] a method has been described in which conformally flat black hole data does indeed lead to the correct Schwarzschild result for the binding energy in the test mass limit. That method is quite different, for example u is approximated by zero and the local masses entering the binding energy are defined differently. At this point it is not clear how to make contact with our approach, but this is clearly an important question for future research.

VIII. CONCLUSION

In Cartesian coordinates the regular part of the conformal factor of puncture initial data is only C^2 differentiable at the punctures. Therefore, a numerical implementation based on a spectral method is expected to be at most fourth-order algebraically convergent. However, one can overcome this problem by introducing appropriate coordinates in which the solution is smooth at the punctures. In particular, our transformation maps the entire $\mathbb{R}^3$ onto a single rectangular domain with the punctures at the boundary.

We have demonstrated rapid convergence of our single-domain spectral method and obtained highly accurate numerical solutions. Moreover, we have provided a comparison to a numerical implementation with finite differences in Cartesian coordinates and found good agreement.

While our coordinate transformation renders puncture data smooth at the punctures, in general the falloff of the extrinsic curvature appears to imply the existence of logarithmic terms such that the solution is only C^4 at infinity if the total linear momentum vanishes, and only C^2 otherwise. This behavior is a consequence of the falloff of the Bowen-York extrinsic curvature and as such unrelated to the puncture construction. It is an interesting but to our knowledge mostly open question which other approaches to construct initial data for black holes share or avoid the problem of logarithmic terms at infinity.

As an application of our spectral method for punctures, we have considered small mass ratios, and the corresponding results approach the test mass limit which was obtained through a semianalytic limiting procedure. Finally, we have computed the binding energy of two punctures in the test mass limit and compared it to the binding energy of a test particle in Schwarzschild spacetime and to binding energies in the equal mass case. We find that in the test mass limit the binding energy per mass deviates from the Schwarzschild result by about 50% at the Schwarzschild ISCO, while the binding energy of two punctures in the equal mass case is close to post-Newtonian results, if the ADM mass at each puncture is used to define the local black hole masses. This should be compared with [44], where by a different method conformally flat black hole data does lead to the proper test mass limit.

The study of specific coordinate transformations might also help in reducing the number of domains that are used by methods for binary black hole excision data. We have started a corresponding investigation based on a coordinate transformation that requires two coordinate patches, and we intend to apply spectral methods. Within the analysis of these data we plan among other things to go

into the matter of possible logarithmic expansion terms of the conformal factor in the context of binary black hole excision data.

ACKNOWLEDGMENTS

It is a pleasure to thank P. Laguna and U. Sperhake for discussions. We are grateful to S. Dain for pointing us to the logarithmic expansion terms of the conformal factor at higher orders. This work was supported by NSF Grants No. PHY-02-18750 and No. PHY-02-44788. We also acknowledge the support of the Center for Gravitational Wave Physics funded by the National Science Foundation under Cooperative Agreement No. PHY-01-14375. M. A. was supported by DFG stipend AN 384/1-1.

[1] G. B. Cook, Living Rev. Relativ. **3**, 5 (2000).
[2] G. B. Cook, M.W. Choptuik, M. R. Dubal, S. Klasky, R. A. Matzner, and S. R. Olivera, Phys. Rev. D **47**, 1471 (1993).
[3] S. Brandt and B. Brügmann, Phys. Rev. Lett. **78**, 3606 (1997).
[4] R. A. Matzner, M. F. Huq, and D. Shoemaker, Phys. Rev. D **59**, 024015 (1999).
[5] H. P. Pfeiffer, G. B. Cook, and S. A. Teukolsky, Phys. Rev. D **66**, 024047 (2002).
[6] W. Tichy, B. Brügmann, and P. Laguna, Phys. Rev. D **68**, 064008 (2003).
[7] G. B. Cook, Phys. Rev. D **50**, 5025 (1994).
[8] T.W. Baumgarte, Phys. Rev. D **62**, 024018 (2000).
[9] H. P. Pfeiffer, S. A. Teukolsky, and G. B. Cook, Phys. Rev. D **62**, 104018 (2000).
[10] G. B. Cook, Phys. Rev. D **65**, 084003 (2002).
[11] E. Gourgoulhon, P. Grandclement, and S. Bonazzola, Phys. Rev. D **65**, 044020 (2002).
[12] P. Grandclement, E. Gourgoulhon, and S. Bonazzola, Phys. Rev. D **65**, 044021 (2002).
[13] W. Tichy and B. Brügmann, Phys. Rev. D **69**, 024006 (2004).
[14] W. Tichy, B. Brügmann, M. Campanelli, and P. Diener, Phys. Rev. D **67**, 064008 (2003).
[15] B. Brügmann, W. Tichy, and N. Jansen, Phys. Rev. Lett. **92**, 211101 (2004).
[16] C. Misner, Phys. Rev. **118**, 1110 (1960).
[17] J. Thornburg, Master's thesis, University of British Columbia, Vancouver, British Columbia, 1985.
[18] J. Thornburg, Classical Quantum Gravity **4**, 1119 (1987).
[19] H. P. Pfeiffer, L. E. Kidder, M. A. Scheel, and S. A. Teukolsky, Comput. Phys. Commun. **152**, 253 (2003).
[20] P. Diener, N. Jansen, A. Khokhlov, and I. Novikov, Classical Quantum Gravity **17**, 435 (2000).
[21] S. H. Hawley and R. A. Matzner, Classical Quantum Gravity **21**, 805 (2004).
[22] D. Brill and R. Lindquist, Phys. Rev. **131**, 471 (1963).
[23] C. Misner and J. Wheeler, Ann. Phys. (N.Y.) **2**, 525 (1957).
[24] R. Beig and N. O'Murchadha, Classical Quantum Gravity **11**, 419 (1994).
[25] R. Beig and N. O'Murchadha, Classical Quantum Gravity **13**, 739 (1996).
[26] R. Beig, gr-qc/0005043.
[27] S. Dain, Phys. Rev. Lett. **87**, 121102 (2001).
[28] J. P. Boyd, *Chebyshev and Fourier Spectral Methods (Second Edition, Revised)* (Dover, New York, 2000).
[29] S. Bonazzola, E. Gourgoulhon, and J.-A. Marck, Phys. Rev. D **58**, 104020 (1998).
[30] S. Bonazzola, E. Gourgoulhon, and J.-A. Marck, Phys. Rev. Lett. **82**, 892 (1999).
[31] M. Ansorg, A. Kleinwächter, and R. Meinel, Astron. Astrophys. **381**, L49 (2002).
[32] M. Ansorg, A. Kleinwächter, and R. Meinel, Astron. Astrophys. **405**, 711 (2003).
[33] K. Schöbel and M. Ansorg, Astron. Astrophys. **405**, 405 (2003).
[34] M. Ansorg, T. Fischer, A. Kleinwächter, R. Meinel, D. Petroff, and K. Schöbel, gr-qc/0402102 [Mon. Not. R. Astron. Soc. (to be published)].
[35] M. Ansorg, A. Kleinwächter, and R. Meinel, Astrophys. J. **582**, L87 (2003).
[36] R. Barrett, M. Berry, T. Chan, J. Dongarra, V. Eijkhout, C. Romine, and H. van der Vorst, *Templates for the Solution of Linear Systems: Building Blocks for Iterative Methods* (SIAM, Philadelphia, 1993), http://www.netlib.org/templates/.
[37] HYPRE—High Performance Preconditioners: http://www.llnl.gov/CASC/hypre/.
[38] S. Dain and H. Friedrich, Commun. Math. Phys. **222**, 569 (2001).
[39] R. J. Gleiser, C. O. Nicasio, R. H. Price, and J. Pullin, Phys. Rev. D **57**, 3401 (1998).
[40] R. J. Gleiser, G. Khanna, and J. Pullin, Phys. Rev. D **66**, 024035 (2002).
[41] P. Laguna, Phys. Rev. D **69**, 104020 (2004).
[42] H. Pfeiffer, Ph.D. thesis, Cornell University, Ithaca, New York, 2003.
[43] B. D. Baker, gr-qc/0205082.
[44] G. Faye, P. Jaranowski, and G. Schäfer, Phys. Rev. D **69**, 124029 (2004).